

Chapter 3

Efficient velocity model evaluation

Building an accurate seismic velocity model is essential for obtaining an acceptable image of the subsurface. When the subsurface is especially complex, for example in geological settings dominated by irregularly-shaped salt bodies, this task becomes particularly challenging. The large contrast between salt and sediment velocities magnifies the effects of inaccurate salt interpretation, resulting in a poor image. Unfortunately, velocity model-building is a time-consuming process that often requires several iterations. A typical salt-interpretation and model-building workflow involves iterative sediment- and salt-flood migrations to identify the top and base of the salt bodies (Mosher et al., 2007). In situations where the top or (especially) base salt interpretation is uncertain or ambiguous, several different salt scenarios may be geologically feasible. Therefore, a means of quickly testing the effects of several different possible velocity models would be extremely useful for judging and refining salt interpretations. In this chapter, I propose a Born modeling and migration scheme that allows for fast remigrations of data synthesized from an initial image, while incorporating prestack velocity information from the initial image's subsurface offset gathers.

An interactive interpretation and imaging environment would be a valuable model-building tool, and several different approaches have been proposed. Wang et al. (2008) introduced a fast migration scheme built on Gaussian beam imaging (Hill, 1990), that

can quickly test different salt scenarios. This method relies on seismic demigration and redatauning of wavefields to reduce the computational expense of migrating with several different velocity models. However, this method operates in the poststack image domain, neglecting velocity information that can be obtained from prestack images, and is limited by the approximations inherent to beam imaging. A similar approach has been proposed using reverse time migration (RTM) in a “layer-stripping” manner (Wang et al., 2011), but this remains too computationally intensive to test more than a very small number of possible models. Chauris and Benjema (2010) have proposed another method using RTM, which aims to reduce computational expense by summing over time-delays in the subsurface rather than sources. However, at present this method has only been demonstrated in two dimensions, and it remains unclear if an extension to 3D is feasible. Finally, fast migrations may also be achieved through the use of simulated datasets derived from an initial image. Guerra (2010) synthesized wavefields using prestack exploding reflector modeling (Biondi, 2006) as a means for performing wave-equation tomography in the image space. While the amount of preprocessing required for the velocity-updating portion of this method, especially in 3D, makes it less appealing for interactive velocity modeling, the idea of using prestack images to synthesize datasets is central to the scheme presented here.

Born modeling (Stolt and Benson, 1986) is based on a single-scattering approximation of the wave equation. By taking advantage of this approximation, we can simulate a new dataset (Tang and Biondi, 2011; Tang, 2011) from an initial image, whose size and acquisition geometry can be selected independently from those of the original dataset. Furthermore, the simulated data can be migrated using generalized sources, drastically reducing the number of shots required. In most of the examples I show, only a single shot is required, allowing for migrations well within an interactive time frame. In order to improve the accuracy of this method, I use a generalized source function derived from subsurface offset gathers of the initial image. This allows for a more accurate and data-driven result than if a simple wavelet were used as the source function; in addition, including non-zero subsurface offset information into this source function incorporates important velocity information available from the initial image. In this way, inaccuracies in the initial velocity model can be identified

and improved in subsequent iterations.

In the following sections, I review the Born modeling methodology and outline the procedure for obtaining the generalized source and receiver wavefields mentioned above. I then demonstrate the method using simple 2D synthetic models. Crosstalk artifacts arising from the modeling procedure limit these examples to isolated image points along subsurface reflectors; however, these tests show that the method can effectively provide information about the effects of different velocity models on an image. Finally, I apply the method to 2D and 3D portions of a field dataset from the Gulf of Mexico. To assist in interpreting the results, I also introduce a quantitative measure of image quality based on the proportion of an image’s energy focused at or near zero subsurface-offset. Even using an initial image created with an intentionally distorted velocity model, the method successfully identifies a more correct model. As we will see in Chapter 4, the efficiency of this method makes it a potentially powerful tool for interactive interpretation and imaging, especially when integrated with model building tools like image segmentation.

METHOD

The goal of the procedure I will describe is to use Born modeling to synthesize a new dataset that is much smaller than the original dataset used to generate an initial migrated image. Since the synthesized data can be “recorded” at any location in x , y , and even z , this procedure is effectively target-oriented. There are three basic steps needed to reach our goal of efficient velocity model evaluation:

1. Generate an areal source function using one or more subsurface offset gathers from the initial prestack image.
2. Using the new source function and a reflectivity model based on the initial image, employ Born modeling to generate a new dataset with acquisition geometry best suited to image the target area.
3. Migrate the simulated data obtained in Step 2, using the source function from

Step 1. This step is extremely computationally efficient compared to a full migration of the original data, allowing for testing of several possible velocity models in a fraction of the time it would take to evaluate them using standard migration techniques.

In the following sections I detail the theoretical basis for each of these steps.

Generalized source function

In conventional modeling and migration, a simple wavelet or plane wave is often used as the source function. However, here we can take advantage of the fact that the procedure described above begins with a migrated image. This allows us to perform post-stack “exploding reflector” (Claerbout, 2005) modeling of a reflector or point diffractor in the subsurface; the upward-continued wavefield can be recorded at any location, and then injected as an areal source function during Born modeling. Mathematically, this areal source is described as

$$S(\mathbf{x}_s, \omega) = \sum_{\mathbf{x}'} \sum_{\mathbf{h}} G_{v_0}^*(\mathbf{x}' - \mathbf{h}, \mathbf{x}_s, \omega) m(\mathbf{x}', \mathbf{h}), \quad (3.1)$$

where $\mathbf{x}_s = (x_s, y_s, z_s)$ are the arbitrarily defined locations where the wavefield will be recorded; \mathbf{h} is the vector of subsurface half-offsets; ω is angular frequency; \mathbf{x}' is the location of the exploding image point in the subsurface; and G_{v_0} is the Green’s function connecting the source to the image point (here, * denotes the adjoint). The Green’s function is computed using the same velocity model (v_0) that was used to image the originally-recorded data, meaning that the recorded wavefield should be independent of the original velocity model choice. However, since this velocity model is unlikely to be correct, the initial image should contain valuable information about the accuracy of this model in the form of subsurface offset gathers. Subsurface offset gathers from true-velocity images will have all energy focused at zero subsurface offset, while an incorrect velocity model will result in a “smearing” of energy to nonzero offsets (Biondi, 2005). Thus, the inclusion of the subsurface offset term \mathbf{h} in

equation 1 is designed to incorporate this information into the modeling. To illustrate the advantage gained by incorporating this information, Figures 3.1(a) and 3.1(b) show two recorded source wavefields from an image point that is actually located at $z = 1000$ in the subsurface, but was initially imaged with a velocity that was 15% too slow. Both recorded wavefields have been reverse-propagated back to zero time to facilitate comparison. The source function in panel (a) was modeled using only the zero subsurface offset $h = 0$ data from the initial image, while the result in panel (b) uses the non-zero offset information as written in equation 1. When only zero subsurface offset data are used, the source appears to focus at the incorrect depth; when the nonzero offset data are used, the effects of using the wrong velocity are apparent. Using the source function in Figure 3.1(b) therefore supplies more useful information for the Born modeling and migration scheme described in the next section.

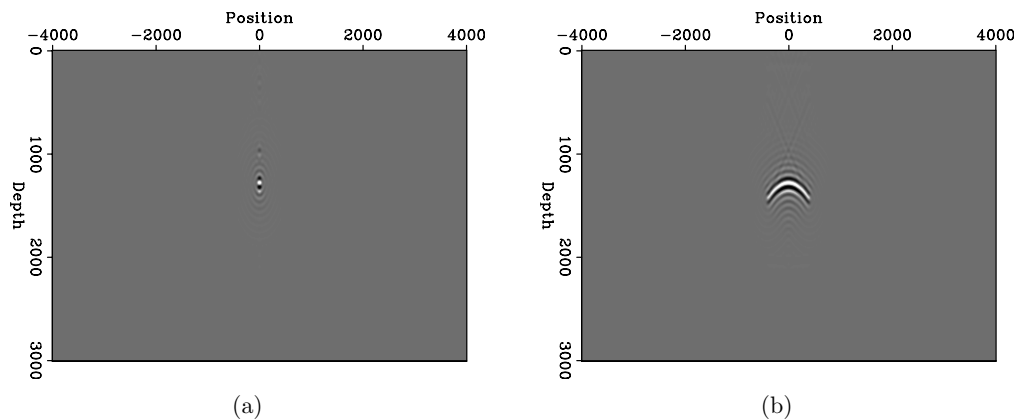


Figure 3.1: Recorded source wavefields that have been reverse-propagated to zero-time; the result in (a) does not include information from the nonzero subsurface offsets of the initial image, while (b) does include this information. Both the initial migration and the modeling used a velocity model that was 15% too slow. [ER]

chap3/. pt-0,pt-n0

Born modeling and migration

I now use the modeled areal source to generate a new data set via Born modeling. To do this, I define the simulated dataset d' recorded at arbitrary receiver locations \mathbf{x}'_r :

$$d'(\mathbf{x}_r, \omega) = \sum_{\mathbf{x}'} \sum_{\mathbf{h}} \Gamma(\mathbf{x}_s, \mathbf{h}, \omega) G_{v_0}(\mathbf{x}' + \mathbf{h}, \mathbf{x}'_r, \omega) m(\mathbf{x}', \mathbf{h}). \quad (3.2)$$

Here, m is the reflectivity model (in our case, the initial image), and the Γ term is defined as

$$\Gamma(\mathbf{x}_s, \mathbf{h}, \omega) = \sum_{\mathbf{x}_s} S(\mathbf{x}_s, \omega) G_{v_0}(\mathbf{x}_s, \mathbf{x}' - \mathbf{h}, \omega), \quad (3.3)$$

where S is as defined in equation 3.1. Crucially, the Green's functions in equations 3.1 and 3.2 are computed using the same velocity model - the one used to generate the initial image. As proven in Tang (2011), this means that the “data” synthesized using equation 3.2 will be kinematically invariant of this initial model. Even though this model is likely to be wrong, we can still confidently make use of the data synthesized from it.

Because the placement of the receiver locations in equation 3.2 can be arbitrarily determined, they do not necessarily need to be on the surface, like the original recorded data. Placing the receivers at depth can improve the efficiency of this method by providing the capability for target-oriented imaging; if a velocity model is well-determined down to a given depth, the synthesized data can be recorded below that depth, avoiding unnecessary computation. This has a similar effect to re-datuming the wavefields, an approach taken by Wang et al. (2008) in their fast image updating strategy.

Now that we have new source and receiver wavefields, we can produce an image using standard wave-equation migration techniques:

$$m'(\mathbf{x}', \mathbf{h}) = \sum_{\omega} G_{v_1}^*(\mathbf{x}' - \mathbf{h}, \omega) \sum_{\mathbf{x}_r} G_{v_1}^*(\mathbf{x}' + \mathbf{h}, \mathbf{x}'_r, \omega) d'(\mathbf{x}_r, \omega). \quad (3.4)$$

It is important to note that this formulation is a conceptual description of wave-equation migration; in practice, a computer propagates the wavefields in discrete time steps and correlates them to form an image. Crucially, the Green’s functions in equation 3.4 can be computed using any velocity model (v_1), and not necessarily the same one used to generate the source and receiver wavefields in previous steps. This can allow for testing of multiple possible velocity models. Furthermore, since subsurface offset gathers are generated during the imaging, we can develop a quantitative means of judging the accuracy of these various models. We expect a “perfect” velocity model to focus all an image’s energy at zero subsurface-offset. Therefore, a simple measure of image quality calculates what proportion of the energy indeed resides at zero or near-zero subsurface-offset:

$$F = \frac{\sum_{i=\mathbf{p}} |A_i|}{\sum_{i=\mathbf{p}} |A_i| \exp(\alpha \frac{|h_i|}{h_{\max}})}, \quad (3.5)$$

where \mathbf{p} is the set of all image points, A_i is the amplitude at a given point, h_i is the subsurface offset at that point, and α is an optional user-specified weighting parameter. Using this measure, a value of $F = 1$ means that all energy is perfectly focused at zero offset; as F decreases toward zero the image becomes progressively less focused. Ideally, a measure such as this one would allow a more rigorous comparison among possible models when a more qualitative comparison fails to yield an obvious result.

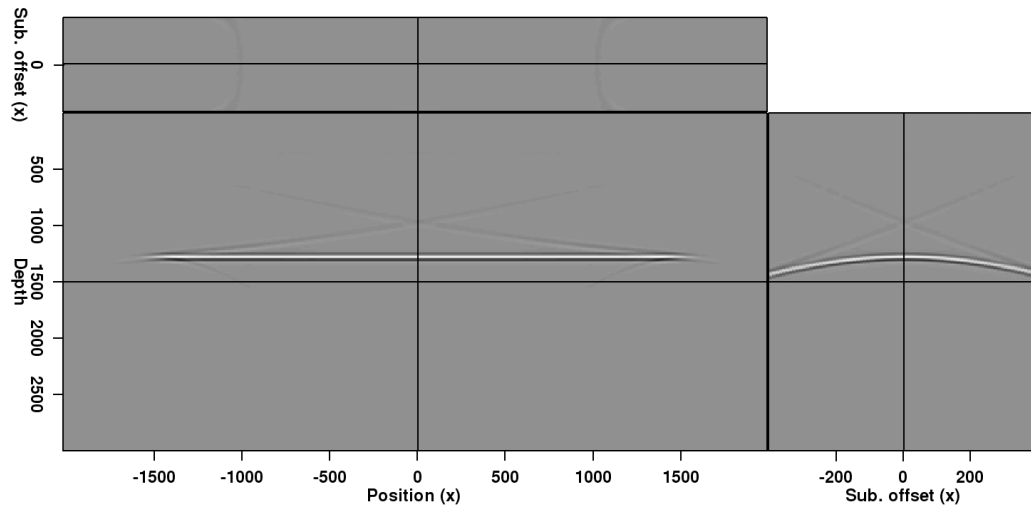
Unfortunately, the imaging procedure as written in equation 3.4 can also generate crosstalk artifacts, since areal source data is used. While various methods such as phase-encoding (Romero et al., 2000; Tang, 2009) are available to help attenuate these artifacts, we restrict our examples in the next section to isolated points in the subsurface, spaced far enough apart to limit the effects of crosstalk. This issue will be explored in more detail in the following sections.

SINGLE-REFLECTOR TESTS

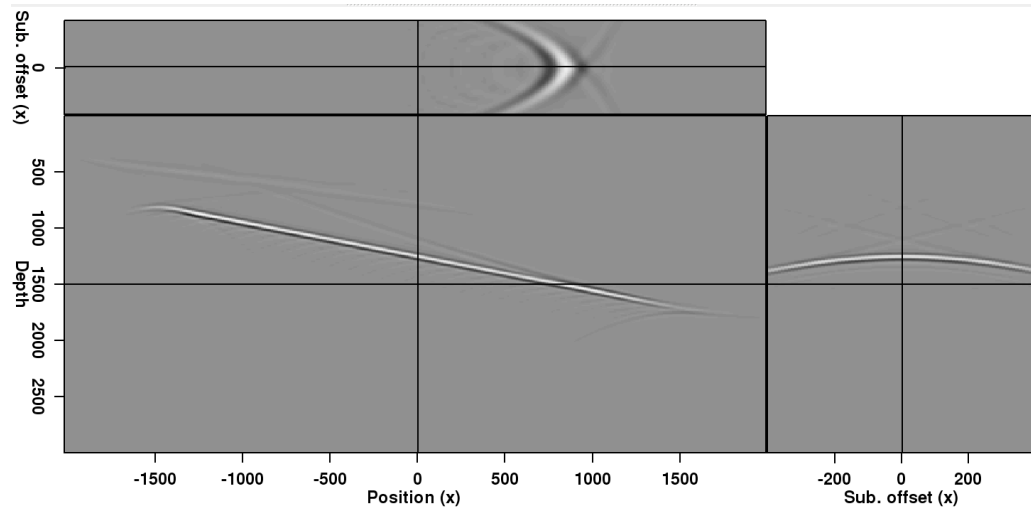
To demonstrate the feasibility of the method outlined above, I will first investigate two simple synthetic test cases: a single flat reflector in the subsurface (Figure 3.2(a)), and a single reflector dipping at 20° (Figure 3.2(b)). Both examples in Figure 3.2 were generated by migrating with an incorrect velocity model (15% slower than the constant-velocity model used to generate the original dataset). The effects of using an incorrect velocity can be seen clearly on the subsurface offset gather (non-focused event). A key goal of the Born modeling procedure is to replicate this behavior when the same velocity model is used to migrate the Born-modeled data. To test this, I sample isolated points from the reflectors in Figure 3.2, and use these points to generate the areal source function described in the previous section. In order to avoid unwelcome crosstalk between these points during the modeling process, they are separated by a distance that is twice the maximum subsurface offset, as seen in Figure 3.3.

Once the source function is “recorded,” Born modeling is performed using the sub-sampled images in Figure 3.3 as reflectivity models. The results of migrating this Born-modeled data, using the same velocity model used to produce the images in Figure 3.2, are seen in Figure 3.4. Because these images were migrated using an areal source function, only a single shot was necessary; this means that the images in Figure 3.4 were produced in seconds, nearly three orders of magnitude less time than was necessary to compute the images in Figure 3.2. Comparing the subsurface offset gathers for both of these figures, we see that while amplitudes differ, the kinematics have been accurately preserved in the Born-modeled result. If our goal is to evaluate the velocity model used, the quickly-obtained results in Figure 3.4 should be sufficient.

As mentioned in the previous section, an advantage of this Born modeling strategy is that the synthesized data may be recorded at any depth, effectively re-datuming wavefields prior to migration. This can lead to significant computational savings, especially if velocities are well known until a certain depth. To verify that this capability does not effect the accuracy of migration results, I recorded both the areal

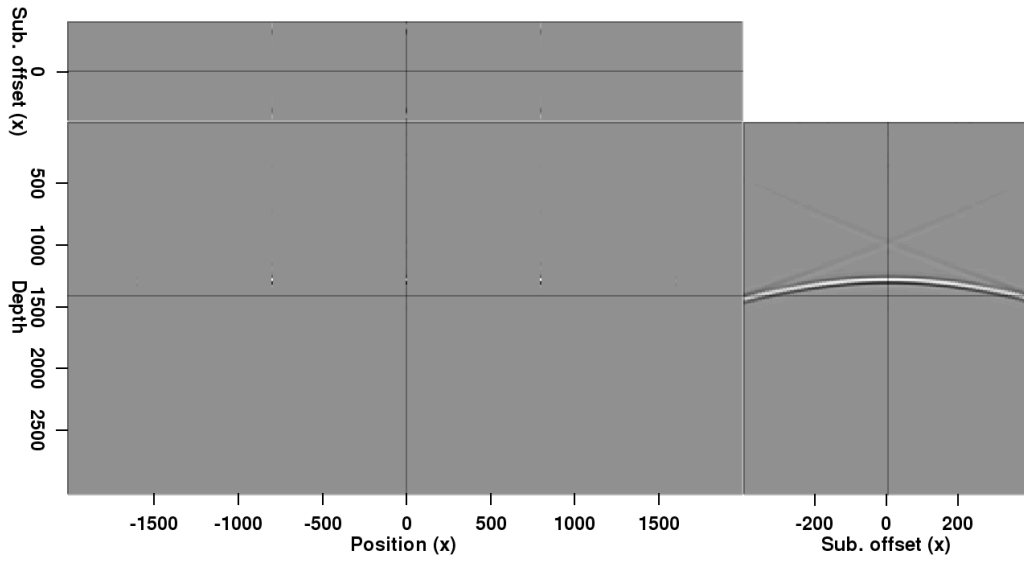


(a)

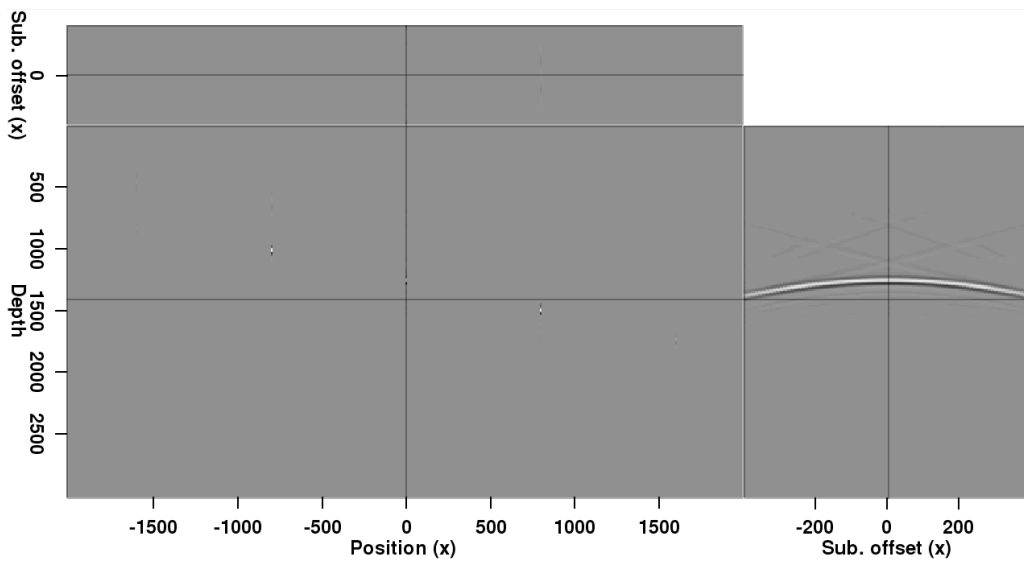


(b)

Figure 3.2: Prestack depth migration images of (a) a flat reflector and (b) a reflector dipping at a 20° angle. The images were migrated with a constant velocity 15% too slow compared to the true velocity, causing the noticeable artifacts and lack of focusing in the subsurface offset dimension. [ER] `chap3/. flat-orig,dip-orig`

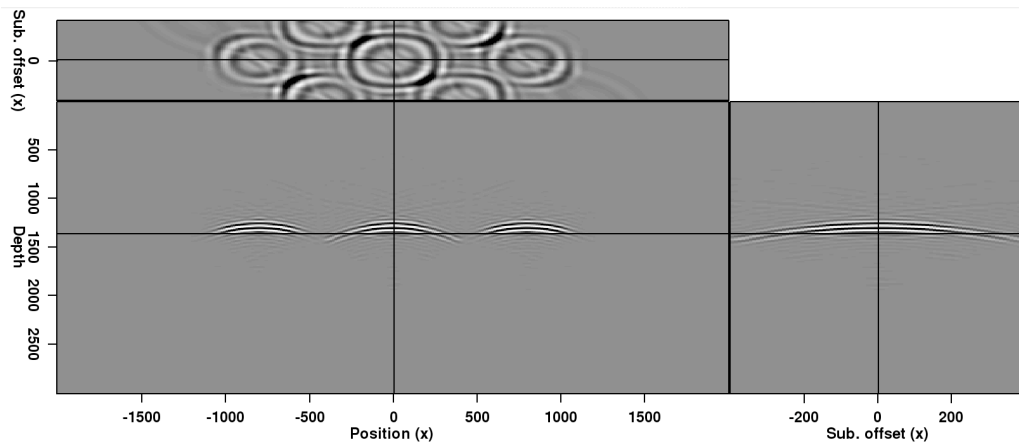


(a)

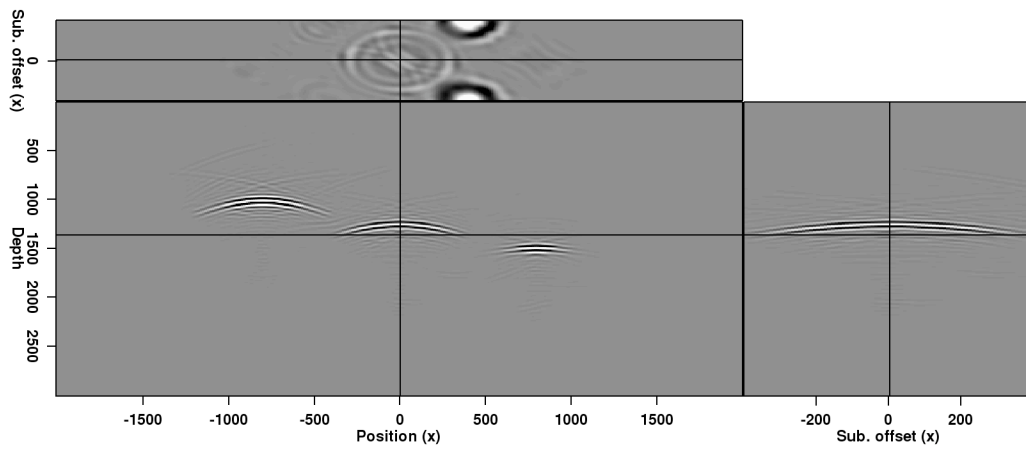


(b)

Figure 3.3: Isolated image points from Figures 3.2(a) and 3.2(b) used for the modeling procedure. The points are separated by twice the maximum subsurface offset value in order to avoid crosstalk artifacts in the modeling. [ER] chap3/. flat-sp,dip-sp



(a)



(b)

Figure 3.4: Migrated images after Born modeling using the images in Figure 3.3 as the reflectivity model. Although the amplitudes differ, the kinematics of the events in both figures match. [ER] chap3/. flat-sp-born,dip-sp-born

source wavefield and the Born-modeled data at depth $z = 750$, instead of at the surface. Figure 3.5 shows the result of migrating this data in the dipping reflector case. Comparison with Figure 3.4(b) confirms that the two results are virtually identical for the area of interest.

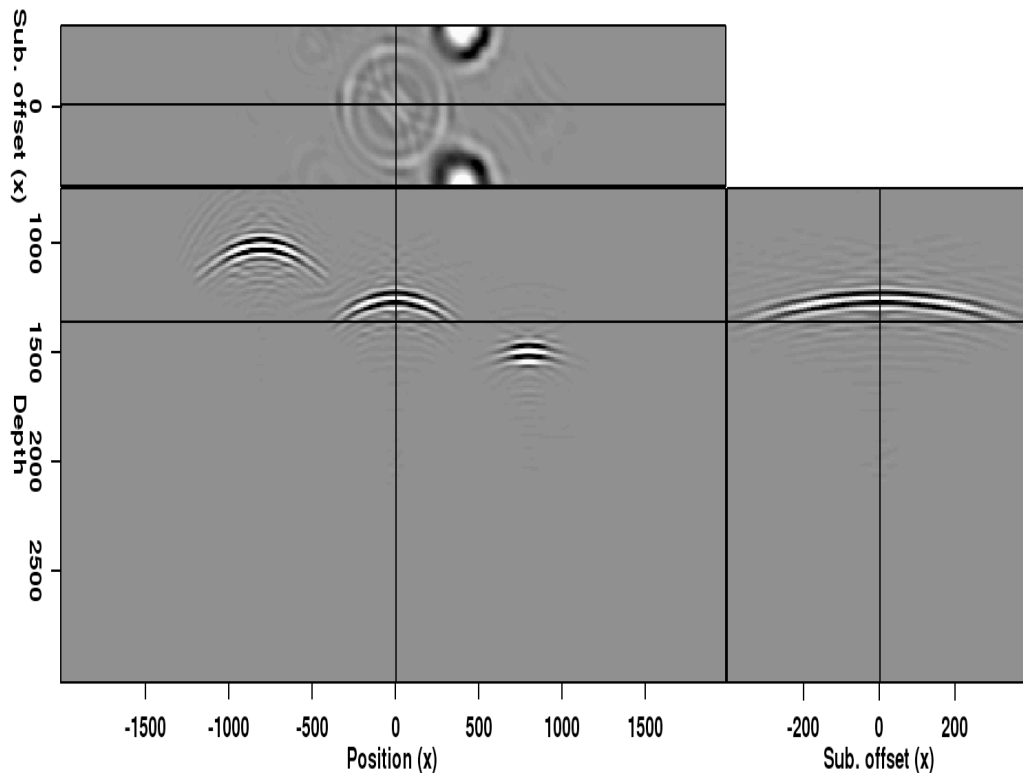


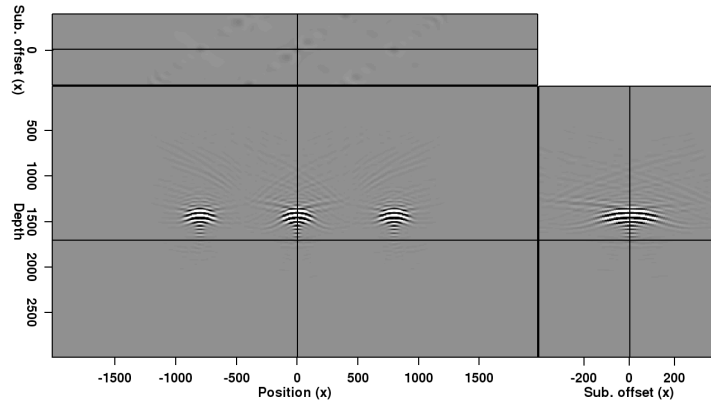
Figure 3.5: Migration result using Born-modeled data from the model in Figure 3.3(b). In this case, the synthesized data was recorded in the subsurface instead of on the surface, effectively re-datuming the wavefields. [ER] chap3/. dip-short

Finally, we wish to test the ultimate purpose of this method: quickly evaluating multiple velocity models. Once the Born-modeled dataset has been synthesized, we can use any velocity model to image the data. Again, we are able to perform these migrations very quickly, on the order of seconds for the examples here. Figure 3.6

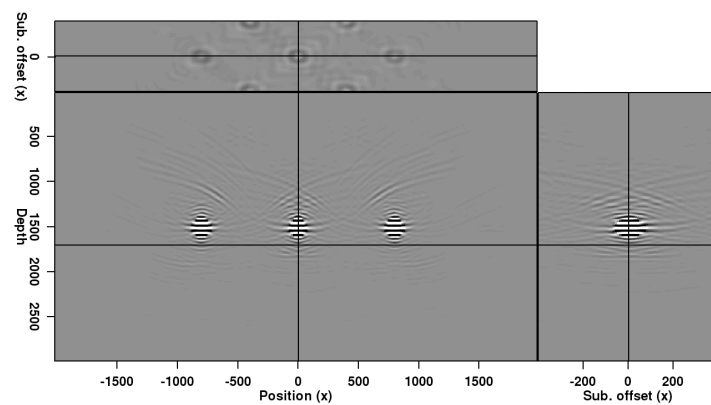
compares the results of using three different velocity models to image the Born-modeled data: one that is 5% slower than the true velocity (Panel a); one that is exactly the true velocity (Panel b); and one that is 5% faster than the true velocity (Panel c). From these results, it is clear that the velocity model used to produce Panel b's result is the most accurate – the subsurface offset gather is flat and relatively focused, and, unlike Panels a and c, there are no signs of over- or under-migration on the zero-subsurface offset image. Because the velocity differences between these three models are relatively small, this is an encouraging sign that this method can ultimately allow us to quickly test more complex models for both synthetic and field data.

Crosstalk mitigation

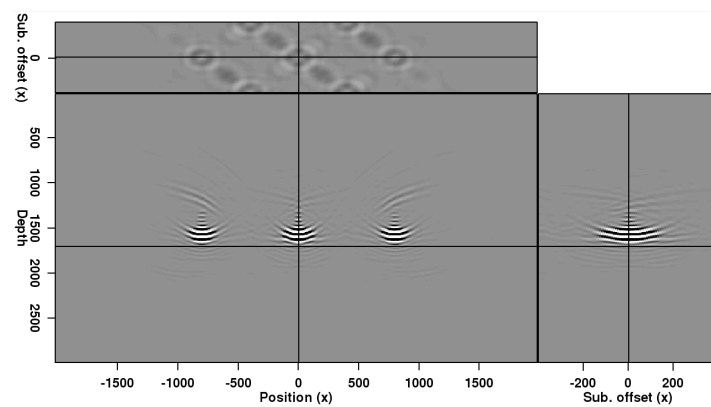
The importance of correctly spacing the image points used for the modeling is illustrated in Figure 3.7. Here, locations from the flat reflector image in Figure 3.2(a) have been sampled twice as frequently, at a spacing equal to the maximum subsurface offset. Figure 3.7 shows the result of using these points to create the areal source function, and then performing Born modeling and migration as before. Now, crosstalk between the closely-spaced image points results in severe artifacts, including spurious events on the zero-subsurface offset image. While the necessity for isolated image locations is a limitation of this method, it can be partially overcome by performing two or more passes of the model evaluation procedure using different image locations. For example, Figures 3.8(a) and 3.8(b) show the results of performing the model evaluation procedure on, respectively, four and three properly-spaced locations from the flat reflector. Taken together, these locations are identical to those used to create the crosstalk-contaminated image in Figure 3.7. However, if the two sets of locations are imaged separately and then summed, the result (Figure 3.8(c)) is free of crosstalk artifacts. While the computational requirements for this method necessarily double for each set of locations imaged in this manner, the advantages gained by obtaining a clearer picture of the reflector may be worth the cost, and still much cheaper than performing full migrations.



(a)



(b)



(c)

Figure 3.6: Result of migrating the Born-modeled data with (a) 5% too slow velocity; (b) correct velocity; and (c) 5% too fast velocity. Each migration was nearly instantaneous, and the effects of the different velocity models are readily apparent. [ER]

chap3/. comp-slow,comp-act,comp-fast

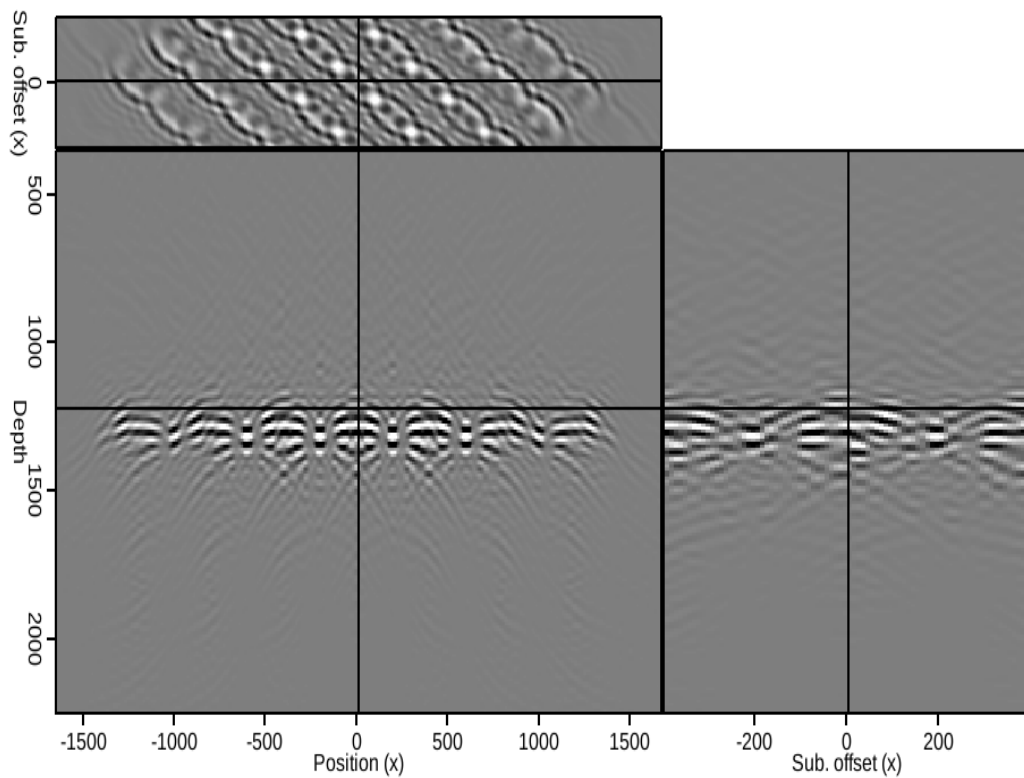
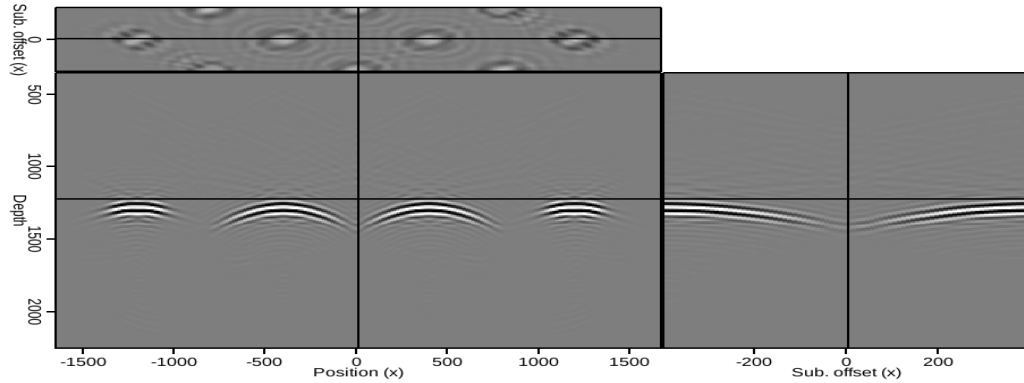
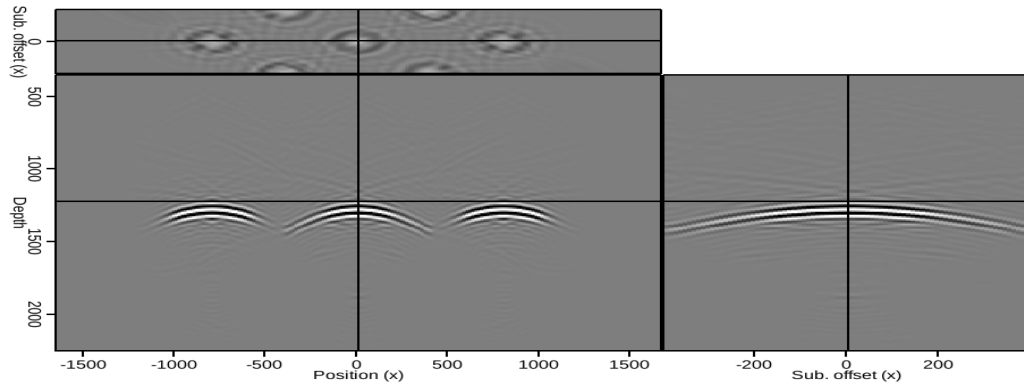


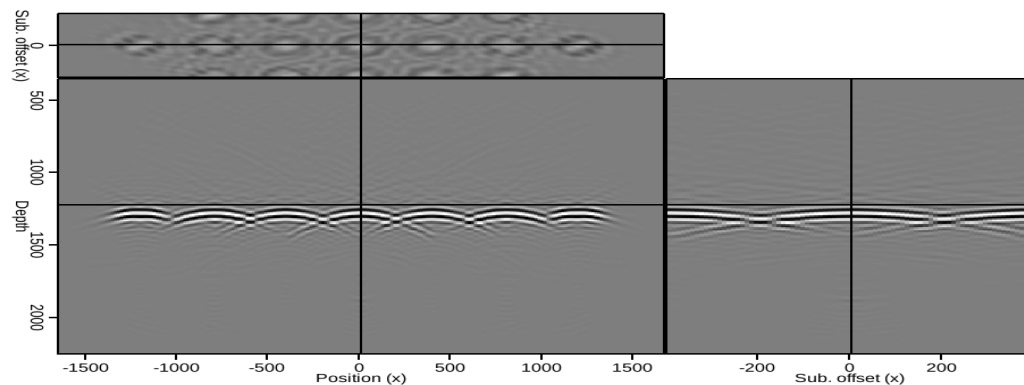
Figure 3.7: Migration result if the image points sampled from Figure 3.2(a) are spaced at less than twice the maximum subsurface offset. Crosstalk artifacts dominate the image, making interpretation extremely difficult. [ER] `chap3/. flat-xtalk`



(a)



(b)



(c)

Figure 3.8: Migration results using (a) four and (b) three image locations sampled from the flat reflector in Figure 3.2(a), and (c) the sum of these two images. Taken together, the sample points in panels (a) and (b) are identical to those used to produce the result in Figure 3.7; however, the image in panel (c) is free of the crosstalk artifacts seen in that result. [ER] chap3/. flat-a,flat-b,flat-sum

Results for a steeply dipping reflector are similar. When multiple, closely-spaced locations along a 40° dipping reflector (Figure 3.9(a)), migrated with a velocity slower than the true velocity, are imaged using a single shot, the result is made uninterpretable by strong crosstalk artifacts (Figure 3.9(b)). However, performing multiple experiments using proper spacing provides a much cleaner, more interpretable result when the images are summed (Figure 3.9(c)). In each of these examples, the slower velocity is used to both generate and image the synthesized wavefields. Taken to the limit, this procedure can even be used to fully reconstruct the reflector, if every location is used to synthesize the wavefields (Figure 3.9(d)). Figure 3.9(d) is not identical to Figure 3.9(a), mainly due to destructive interference of the “frowning” events in both the subsurface offset domain and at zero subsurface offset. A further option to help mitigate this interference is to restrict the subsurface offset domain data used to synthesize the source and receiver wavefields to only a few, specific offset values. The wavefields used to obtain the image in Figure 3.10(a) were generated using only data from $h = -200$, $h = 0$, and $h = 200$ for each x -location along the reflector in Figure 3.9(a). Now, not only is the reflector fully reconstructed at zero subsurface offset, but there is clear evidence in the subsurface offset gather that the velocity used was indeed too slow. Imaging the wavefields instead with the true velocity (Figure 3.10(b)) correctly yields an image focused at zero subsurface offset. Furthermore, the reduction in interference allows for a more faithful reconstruction of the original reflector in both Figures 3.10(a) and 3.10(b) than was possible in Figure 3.9(d), for which all the subsurface offset domain data were used.

This result suggests that particular care should be taken when applying this method to steeply dipping reflectors; however, the interpreter-driven nature of the workflow makes it simple for analysis to be constrained to relatively flat portions of a reflector if necessary. In any case, the accurate reconstruction of even the dipping reflector provides further evidence of the advantages of synthesizing multiple wavefields to image different parts of the reflector. The remaining examples in this chapter are limited to a single set of locations per reflector, but the 3D field data example in Chapter 4 will take advantage of this “split-and-sum” strategy.

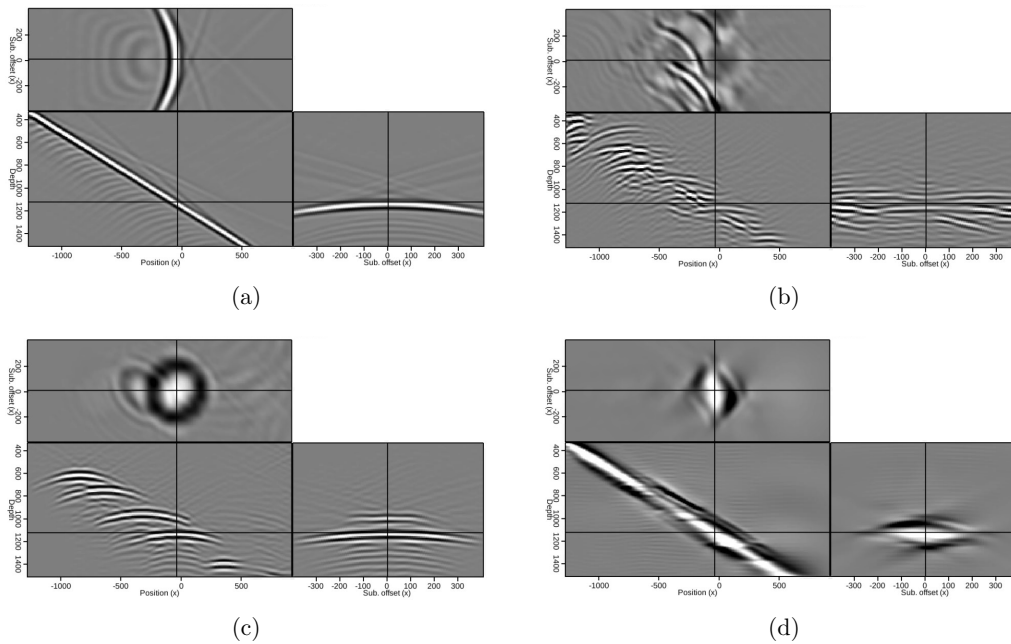
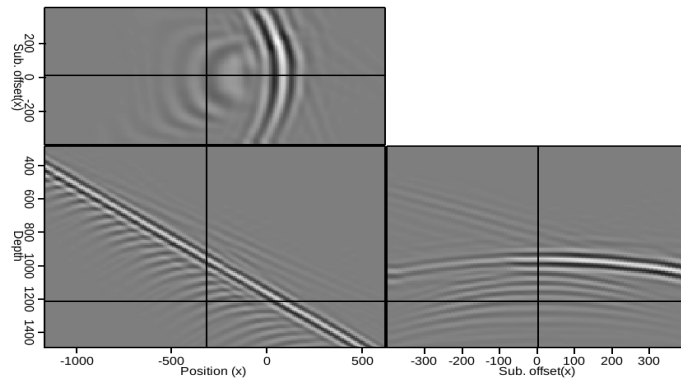
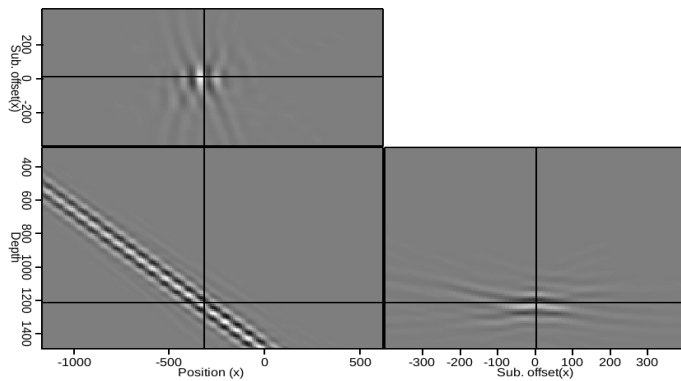


Figure 3.9: (a) Initial image of a 40° dipping reflector; (b) crosstalk-contaminated result of using a single source function derived from closely spaced locations along the reflector; (c) result of summing several images generated using wavefields synthesized from properly-spaced locations along the reflector; (d) full reconstruction of the reflector after using all locations along the reflector to synthesize wavefields and summing the individual results. [CR] chap3/. dip2,dip-xtalk,dip-cmb,dip-full



(a)



(b)

Figure 3.10: Results of imaging wavefields synthesized using every location along the reflector in Figure 3.9(a), but restricting the use of subsurface offset information to three offsets only ($h = 0, \pm 200$). In (a), the slow velocity was used to migrate the wavefields, while the true velocity was used in (b). [CR]

chap3/. dip-sel-slow,dip-sel-true

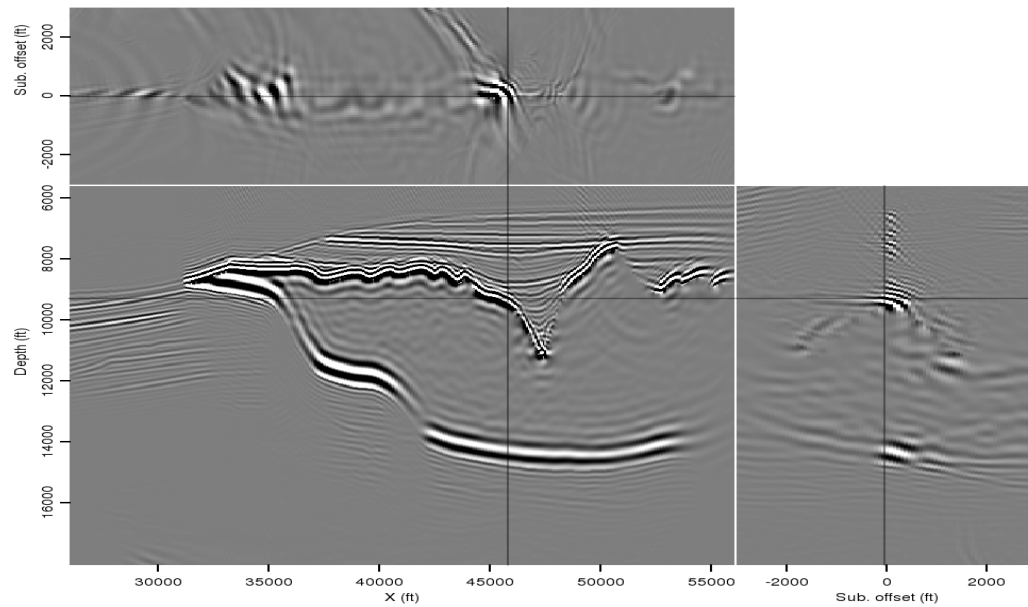
2D SYNTHETIC EXAMPLE

The above procedure will now be demonstrated using two different initial images derived from the Sigsbee synthetic model. Figure 3.11(a) is a perfect-velocity, full migration of the Sigsbee data, which will be used for the first example. Figure 3.11(b) shows a manually-picked reflector chosen for further analysis; in this case, the base salt has been chosen because it should be particularly sensitive to different interpretations of the salt body’s shape and velocity, the two model variations that will be tested. Finally, Figure 3.12 shows two image locations isolated from the selected reflector. Note that most of the energy is focused near zero subsurface-offset, since the true velocity model was used for the initial image.

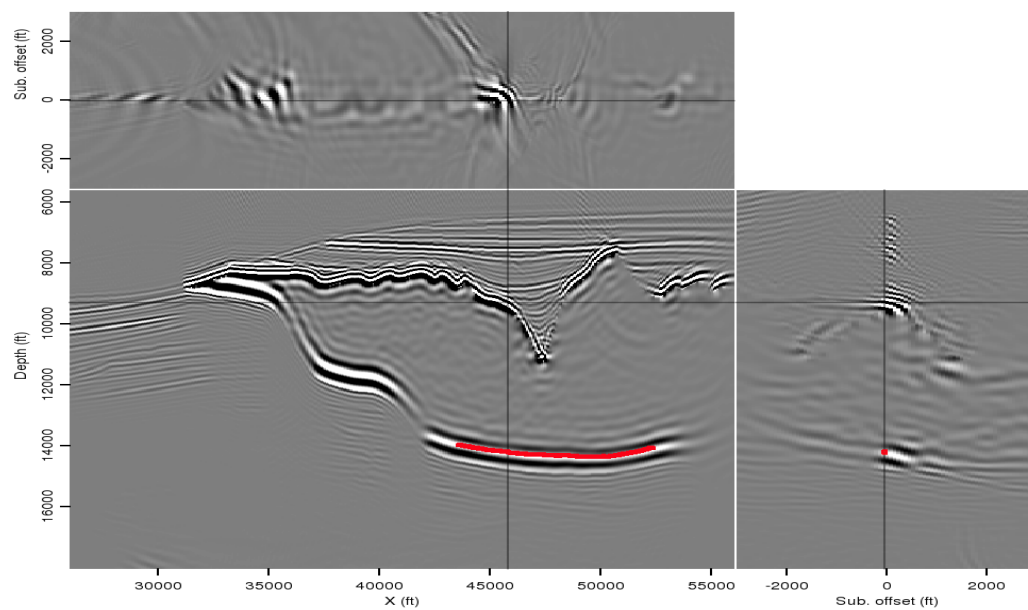
After synthesizing the source and receiver wavefields as described in the previous section, the new wavefields were imaged using three different velocity models. First, the true model, seen in Figure 3.13(a). Second, an alternative model created via automatic image segmentation, in which an interpreter has chosen to include an extra chunk of salt (Figure 3.13(b)). The third model tested was identical to the true model in salt shape, but with a salt velocity 5% slower than the true model.

Resulting images from the Born-modeled data are seen in Figure 3.14. Panel 3.14(b), the result of migrating with the extra-salt model in Figure 3.13(b), is clearly the least well-focused image. However, it is difficult to qualitatively distinguish between the other two results. Instead, the results of calculating the F value from equation 3.5 can provide a quantitative comparison of the images in Figure 3.14. These calculations are found in table 3.1; as expected, the result using the true model has a higher F value, indicating it is more well-focused.

The second example uses an initial image created with an incorrect velocity model; in this case, the “slow salt” model described above. The results corresponding to each velocity model can be seen in Figure 3.15. Again, the extra-salt model is clearly inferior, but the differences between the other two results are more subtle. The F -value calculations in table 3.2 confirm that the true model yields the optimal result, even though the slow-salt model was used to create the initial image and both synthesized



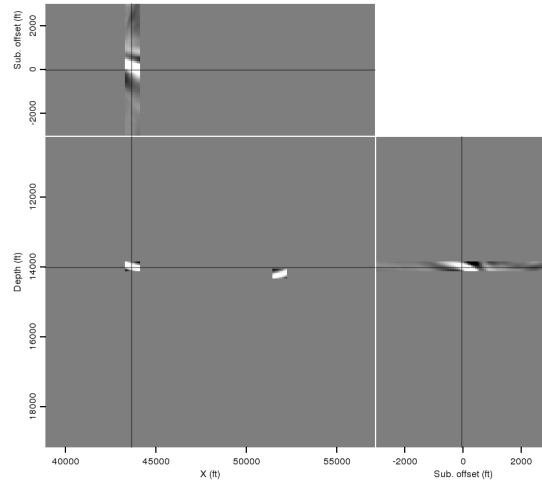
(a)



(b)

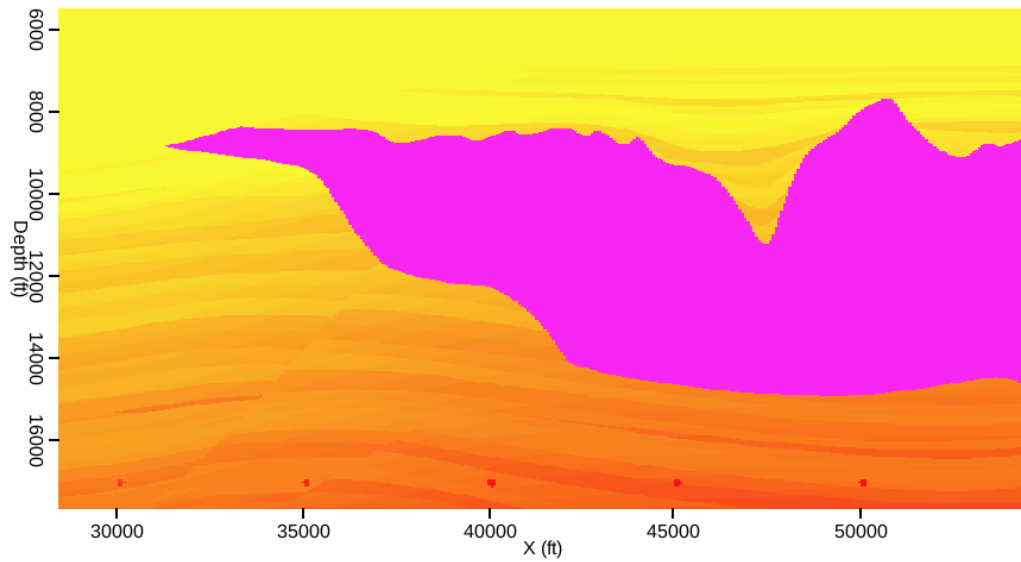
Figure 3.11: (a) A true velocity image using data from a section of the Sigsbee synthetic model; and (b) a base-of-salt reflector selected for further analysis because of its sensitivity to changes in the salt interpretation. [CR] chap3/. img-act,picks

Figure 3.12: Isolated image locations selected from the reflector picked in Figure 3.11(b). [CR]
 chap3/. act-pts

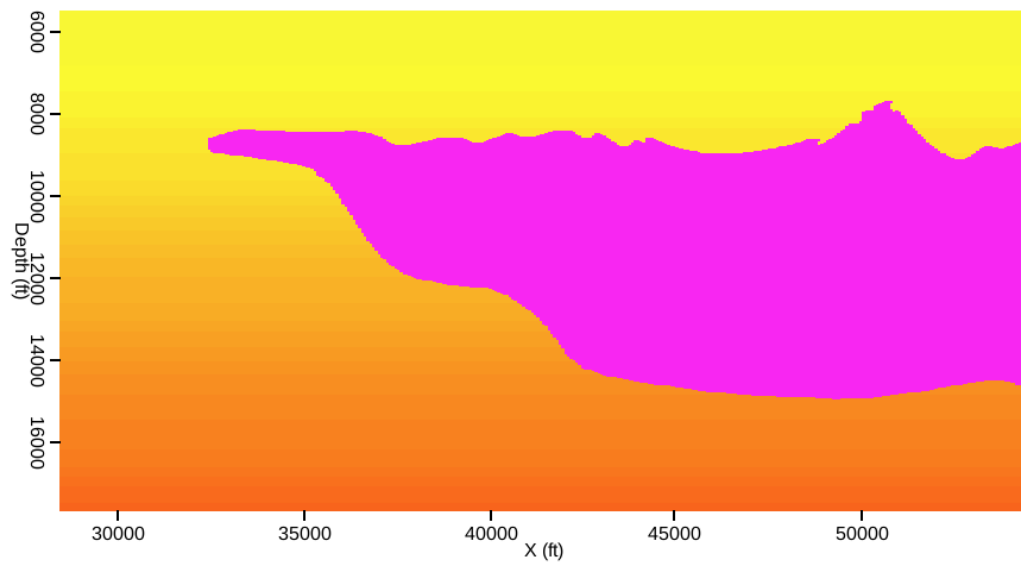


Migration model	F value
True velocity	0.883
Extra salt	0.879
Slow salt	0.864

Table 3.1: Calculations from equation 3.5 for each migration velocity model, after the initial image and synthesized wavefields were created using the true velocity model.



(a)



(b)

Figure 3.13: Two different velocity models to be tested. The model in (a) is the true Sigsbee model, while (b) is an alternate model created by one possible automatic segmentation of the initial image. [ER] `chap3/. zvel-act,zvel-filled`

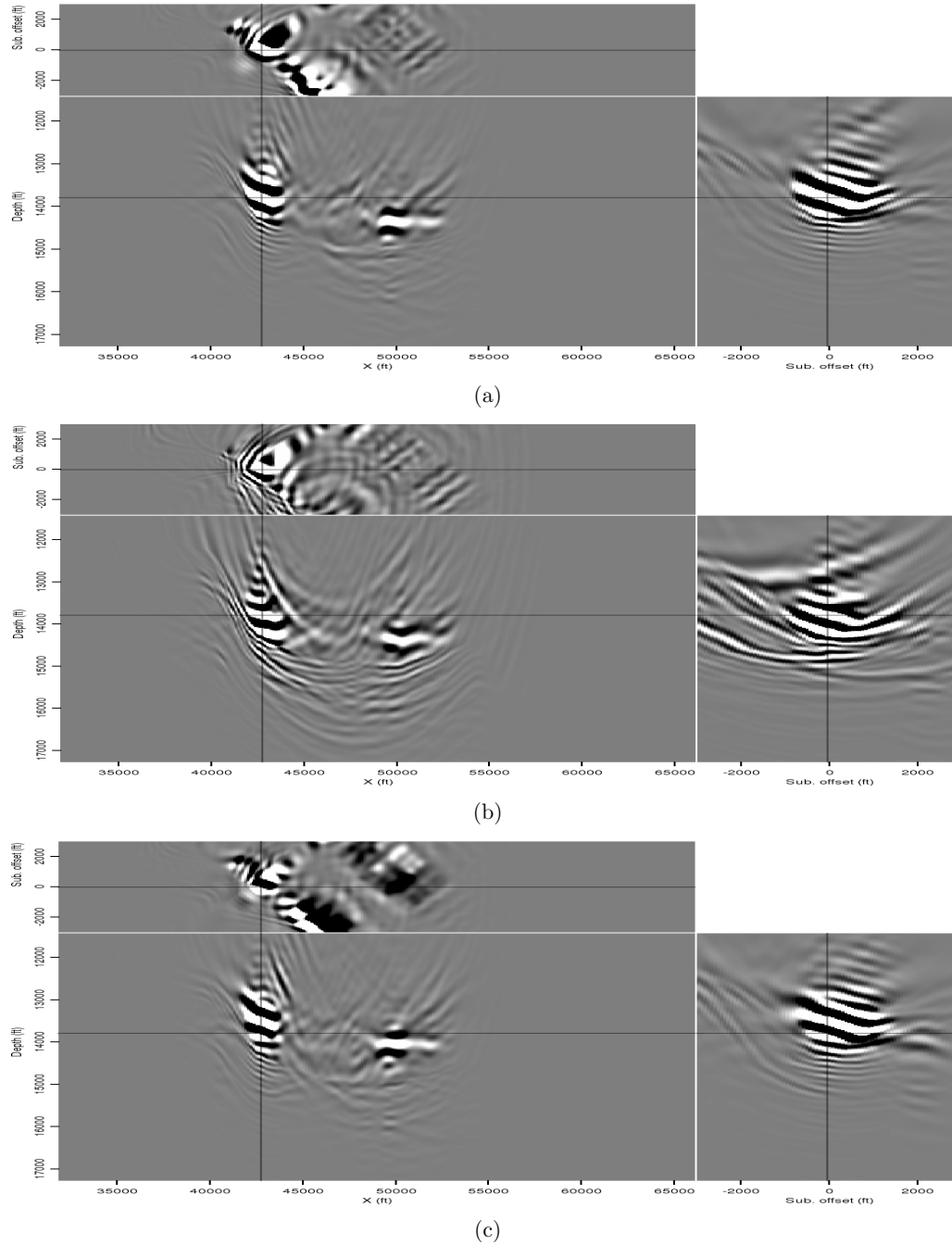


Figure 3.14: Three images of the Born-modeled data using three different migration velocity models: (a) the true model; (b) the extra-salt model; and (c) the slow-salt model. In this example, the initial image was created with the true model. [CR]

chap3/. born-act1,born-af,born-as

Migration model	F value
True velocity	0.621
Extra salt	0.561
Slow salt	0.613

Table 3.2: Calculations from equation 3.5 for each migration velocity model, after the initial image and synthesized wavefields were created using the “slow salt” velocity model.

datasets.

2D FIELD DATA EXAMPLE

The 2D and 3D images used to demonstrate this method are derived from a wide-azimuth Gulf of Mexico dataset provided by Schlumberger Multisclient. Figure 3.16(a) is a 2D migration of a portion of this dataset, imaged using the velocity model provided with the data. To test the method, a single location along the reflector highlighted in Figure 3.16(b) was isolated and used to synthesize the source and receiver wavefields as described previously.

Figure 3.17 shows the results of imaging the new, synthesized wavefields with three different velocity models: the one provided with the data, and models scaled +/- 5% from the one provided. A qualitative examination suggests that the provided model produces the best-focused image, seen in panel (b). A more quantitative analysis using equation 3.5 confirms this; the F -values calculated for each of the images in Figure 3.17 are found in table 3.3.

A more interesting test case is one in which the initial image was not generated using the provided velocity model. The image in Figure 3.18(a) was created using the slower velocity model of the previous example; a location isolated from the reflector indicated in Figure 3.18(b) was used to synthesize the new source and receiver wavefields. The same reflector is chosen in Figure 3.18(b) as in Figure 3.16(b), although the location is slightly shifted due to the difference in velocity models. Now,

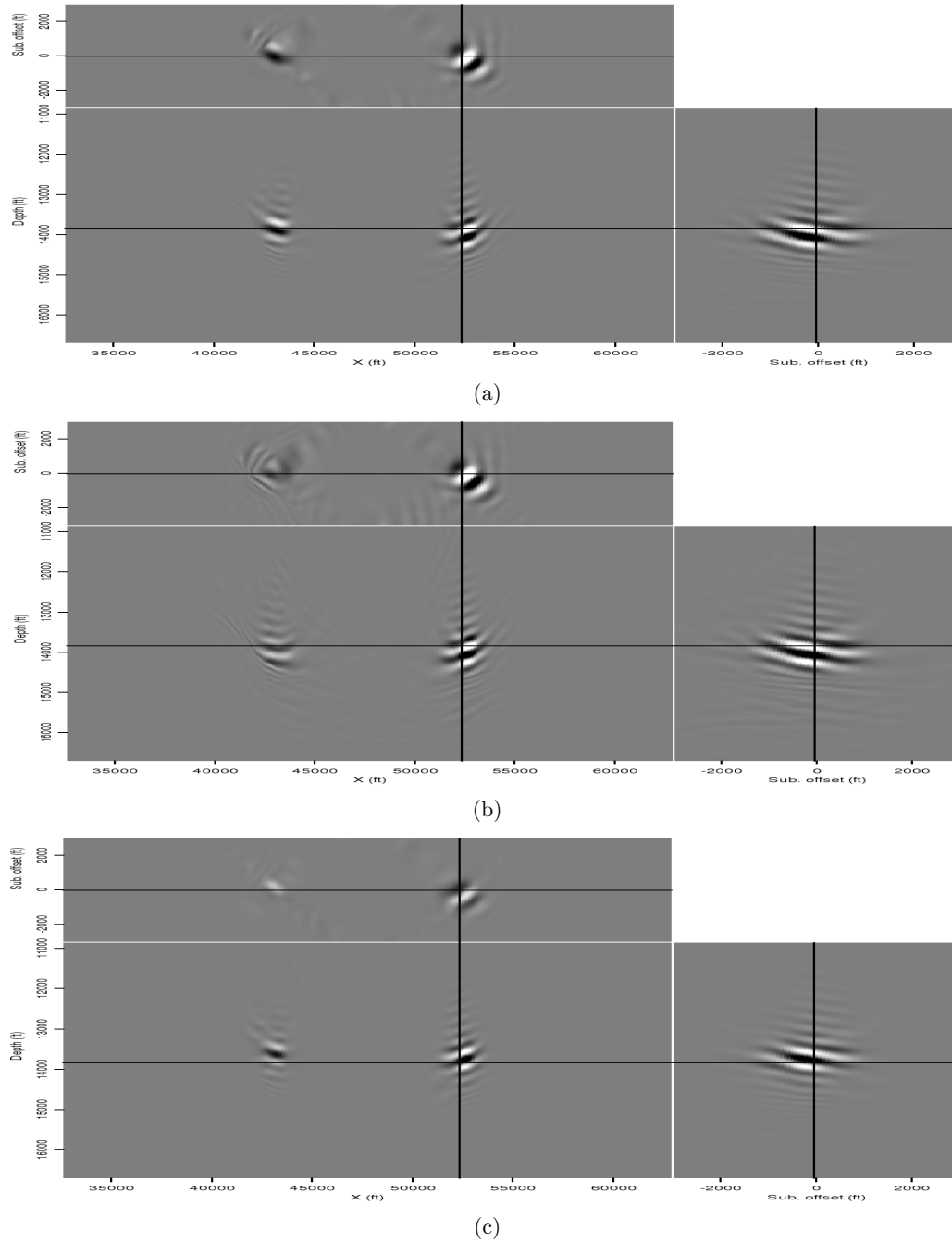
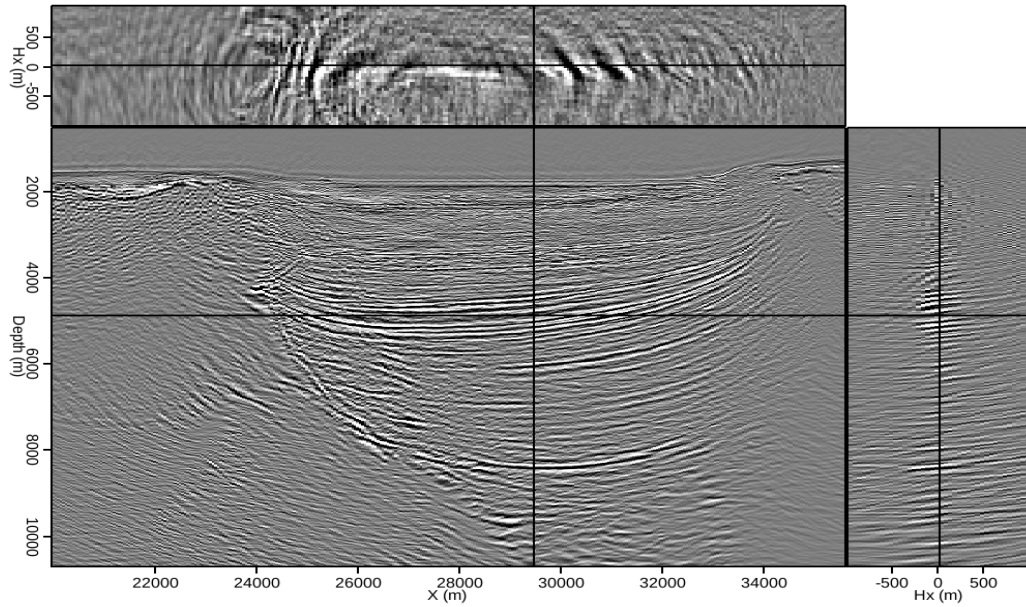
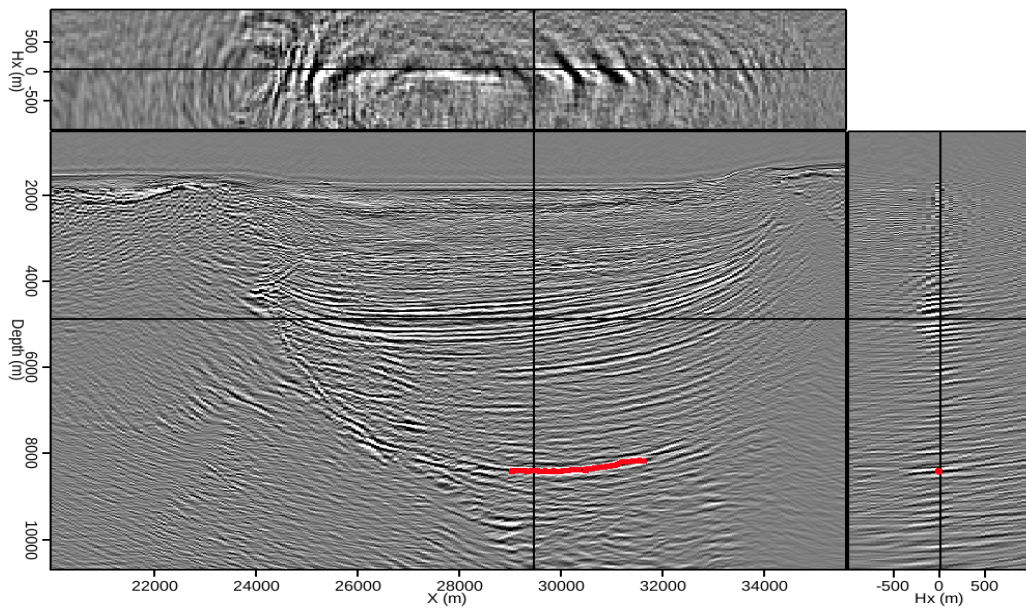


Figure 3.15: Three images of the Born-modeled data using three different migration velocity models: (a) the true model; (b) the extra-salt model; and (c) the slow-salt model. In this example, the initial image was created with the slow-salt model. [CR]

chap3/. born-sa,born-sf,born-ss



(a)



(b)

Figure 3.16: (a) A 2D field image produced using the provided velocity model, and (b) a manually-picked horizon of interest used to test three different velocity models.

[CR] chap3/. 2d-field,act-picks

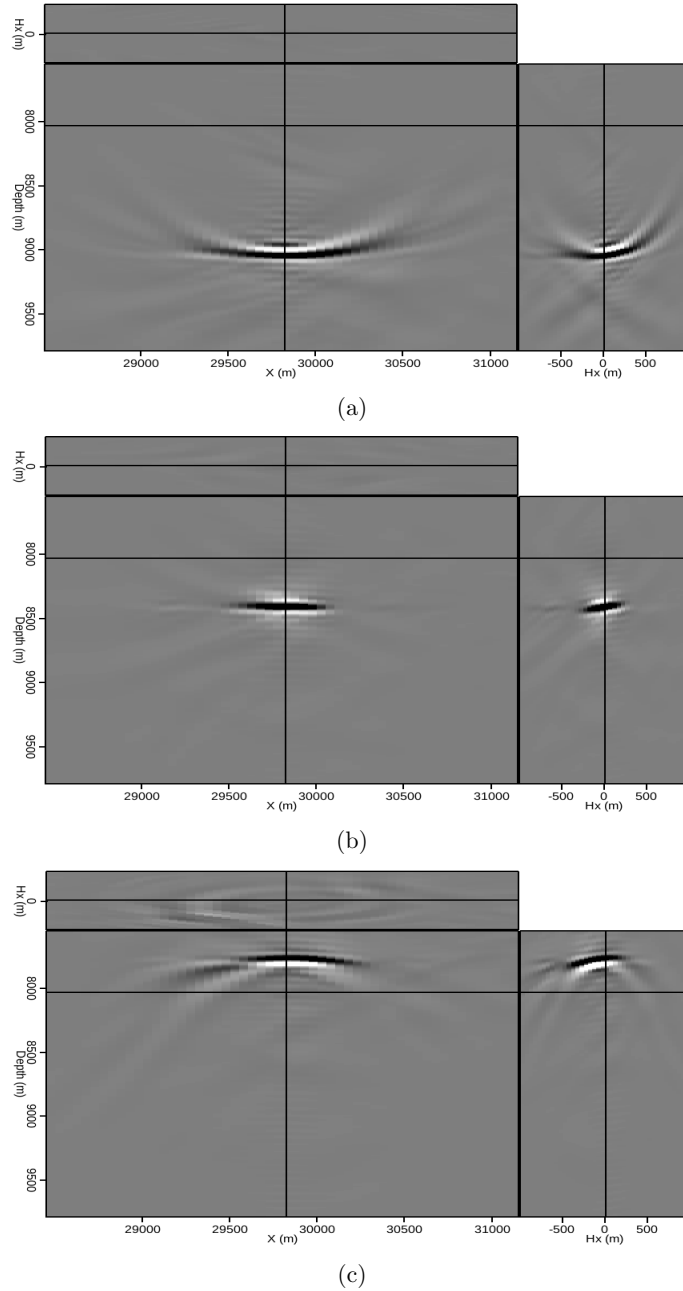


Figure 3.17: A single location from the reflector indicated in Figure 3.16(b), imaged using synthesized source and receiver wavefields and (a) a velocity model 5% faster than the one provided; (b) the provided velocity model; and (c) a model 5% slower than the one provided. [CR] chap3/. born-fast,born-act,born-slow

Migration model	F value
Provided velocity	0.89
Fast model	0.86
Slow model	0.85

Table 3.3: Calculations from equation 3.5 for each 2D migration velocity model, after the initial image and synthesized wavefields were created using the provided velocity model.

Migration model	F value
Provided velocity	0.92
Fast model	0.89
Slow model	0.89

Table 3.4: Calculations from equation 3.5 for each 2D migration velocity model, after the initial image and synthesized wavefields were created using a model 5% slower than the one provided.

Figure 3.19 shows the results of imaging the synthesized wavefields from this initial image, with the same three models as the previous example. Again, the provided model (panel b) delivers the most well-focused result, both qualitatively and quantitatively (from the F -value results in table 3.4). This demonstrates that the method can identify a more accurate model using field data, even when the initial model is less accurate.

3D field data example

Finally, initial tests on 3D data were performed using the same strategy as in the previous section. Figure 3.20(a) shows a relatively small image cube derived from the same Gulf of Mexico dataset used for the 2D examples, and imaged using the provided velocity model. Again, a single location from the manually-interpreted reflector (this time, a 3D horizon) shown in Figure 3.20(b) was used to synthesize 3D areal source and Born-modeled receiver wavefields. Because the prestack image cubes resulting

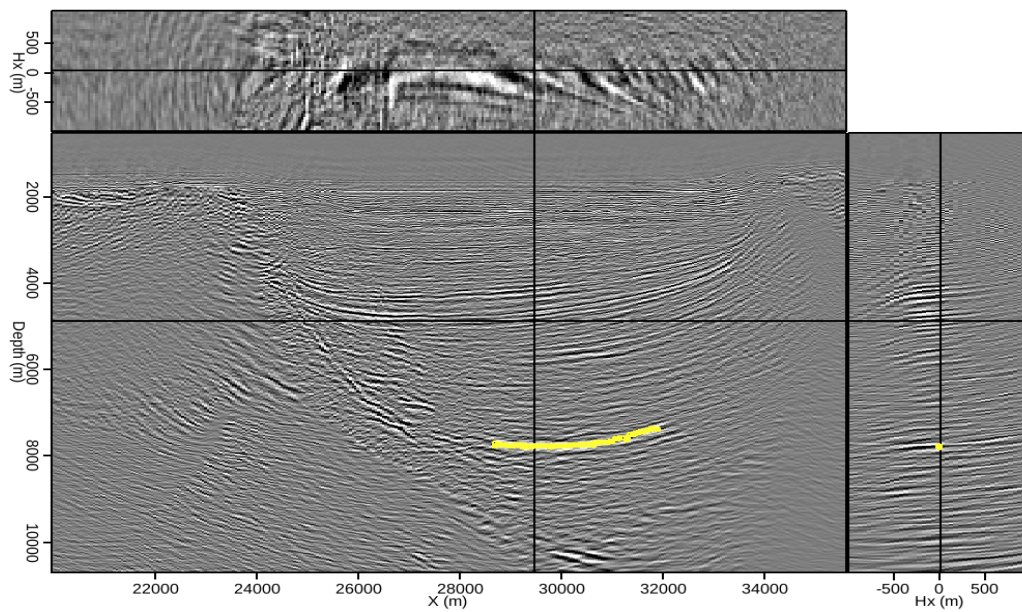
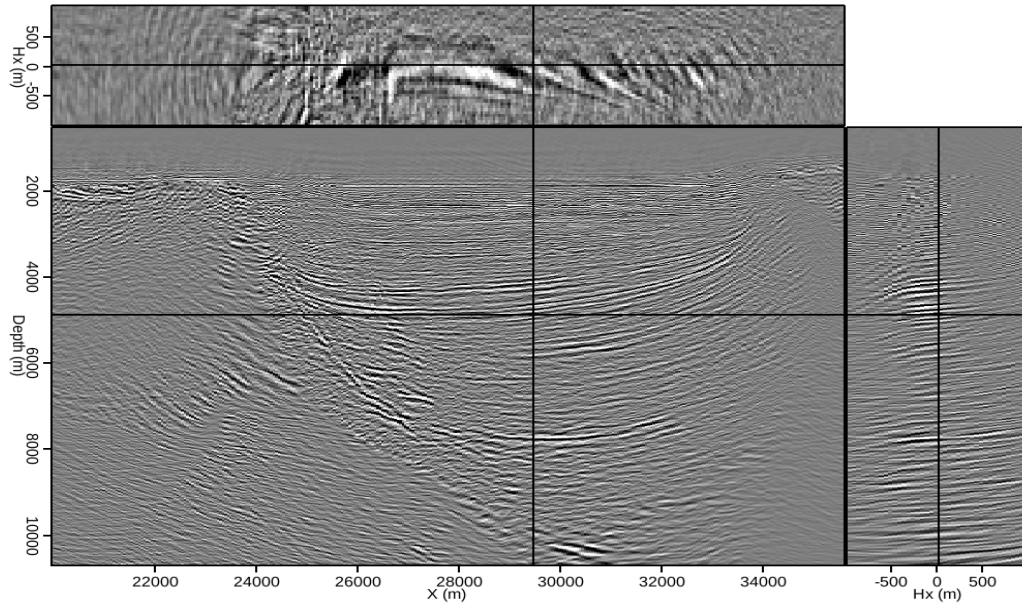
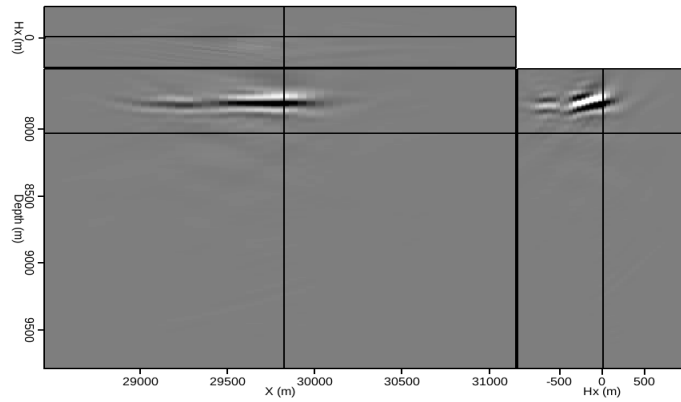
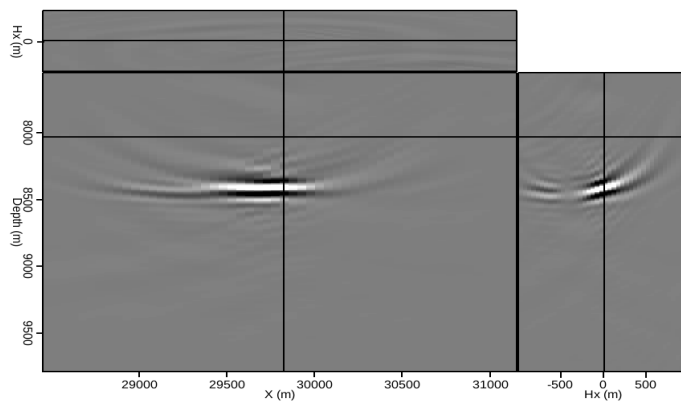


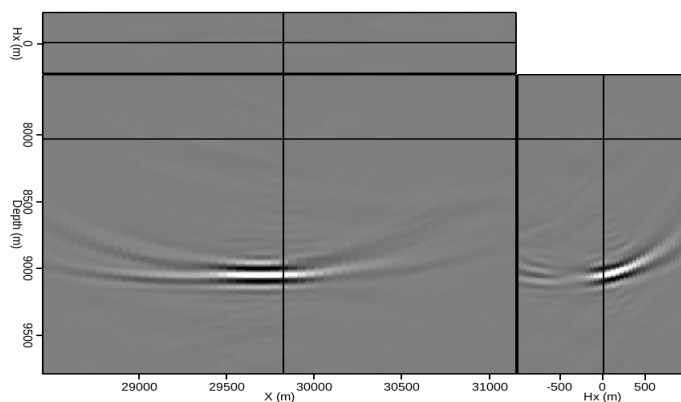
Figure 3.18: (a) A 2D field image produced using a velocity model 5% slower than the one provided, and (b) a manually-picked horizon of interest used to test three different velocity models. [CR] chap3/. 2d-slow,slow-picks



(a)



(b)



(c)

Figure 3.19: A single location from the reflector indicated in Figure 3.18(b), imaged using synthesized source and receiver wavefields and (a) a velocity model 5% slower than the one provided; (b) the provided velocity model; and (c) a model 5% faster than the one provided. [CR] chap3/. slow-slow,slow-act,slow-fast

Migration model	F value
Provided velocity	0.550
Fast model	0.514
Slow model	0.518

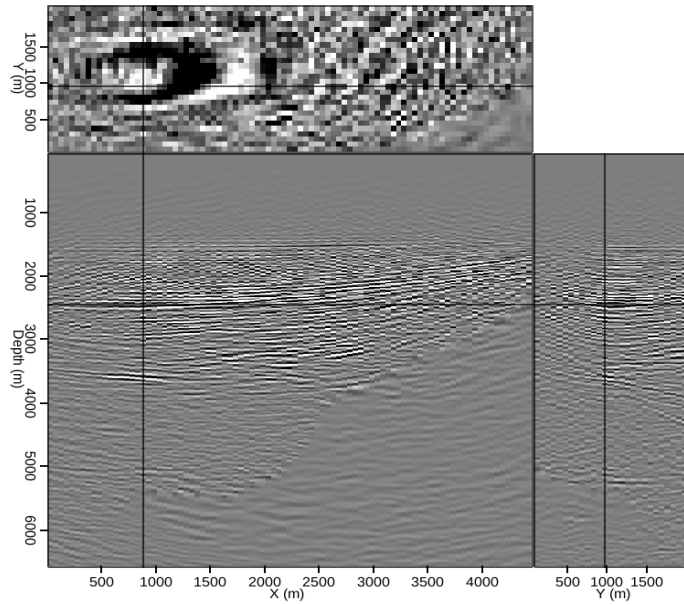
Table 3.5: Calculations from equation 3.5 for each 3D migration velocity model, after the initial image and synthesized wavefields were created using the velocity model provided with the data.

Migration model	F value
Provided velocity	0.481
Fast model	0.470
Slow model	0.466

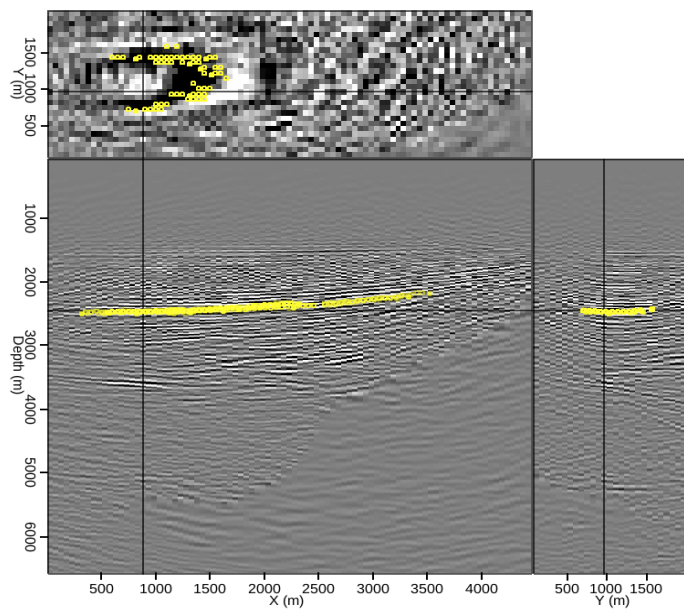
Table 3.6: Calculations from equation 3.5 for each 3D migration velocity model, after the initial image and synthesized wavefields were created using a velocity model 5% faster than the one provided with the data.

from the imaging of these wavefields are five-dimensional, the results are displayed as two separate figures. Figure 3.21 shows images extracted from the cube at zero-subsurface offset in both the x and y directions, after migrating the synthesized wavefields with the three velocity models used for the 2D examples. Figure 3.22 shows the corresponding images in subsurface offset coordinates, extracted at the indicated locations in Figure 3.21. In this example, the image generated using the provided velocity model (panel (b)) appears better focused in both domains. The 3D F -value calculations in table 3.5 provide more quantitative evidence.

The more realistic case of an initial image created using the faster velocity model also yielded encouraging results. While it is slightly more difficult to qualitatively distinguish the best-focused model either at zero-subsurface offset (Figure 3.24) or in the subsurface offset domain (Figure 3.25), the calculations in table 3.6 reveal that the provided model is indeed superior. This example demonstrates the value of a quantitative image focusing measure, especially for difficult-to-visualize 5D volumes.



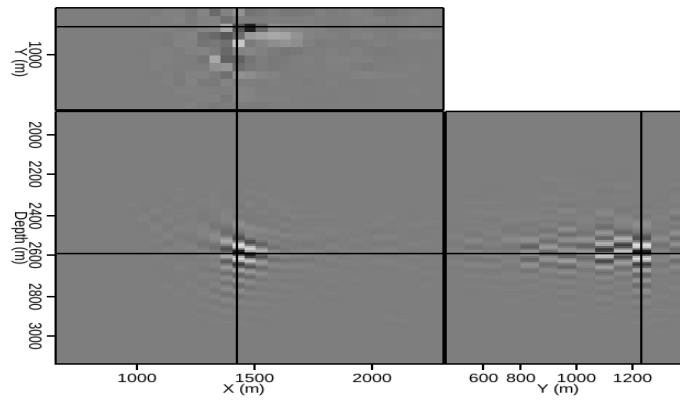
(a)



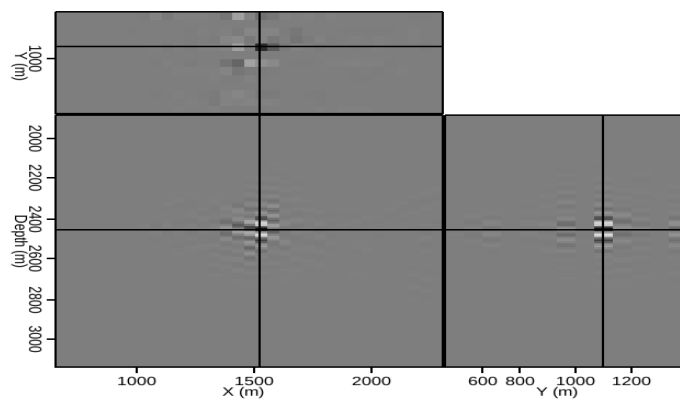
(b)

Figure 3.20: (a) A 3D field image produced using the provided velocity model, and (b) a manually-picked horizon of interest used to test three different velocity models.

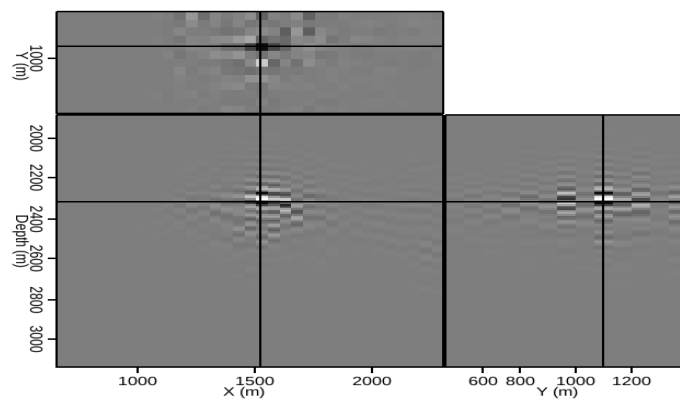
[CR] `chap3/. 3d-field,3d-act-picks`



(a)



(b)



(c)

Figure 3.21: A single location from the reflector indicated in Figure 3.16(b), imaged using synthesized source and receiver wavefields and (a) a velocity model 5% faster than the one provided; (b) the provided velocity model; and (c) a model 5% slower than the one provided. [CR] `chap3/. born-fast3d,born-act3d,born-slow3d`

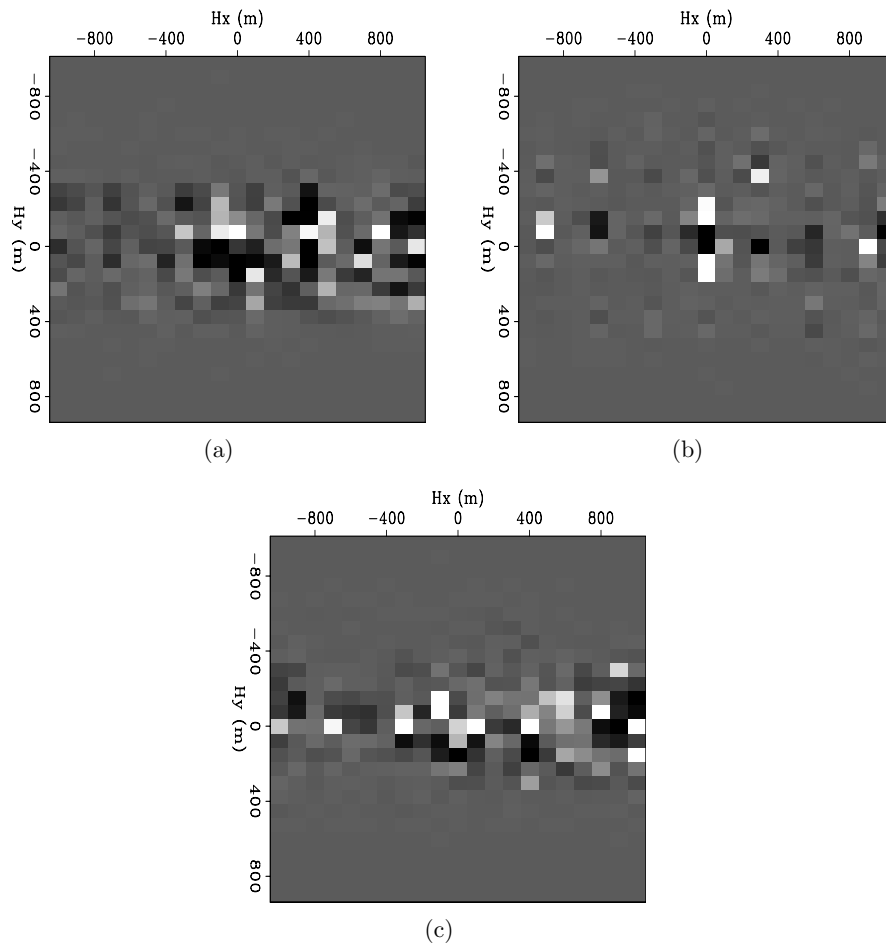
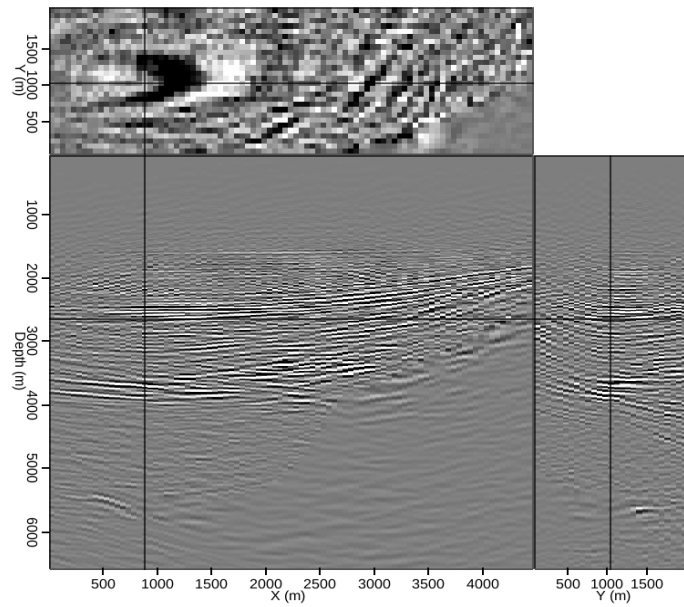
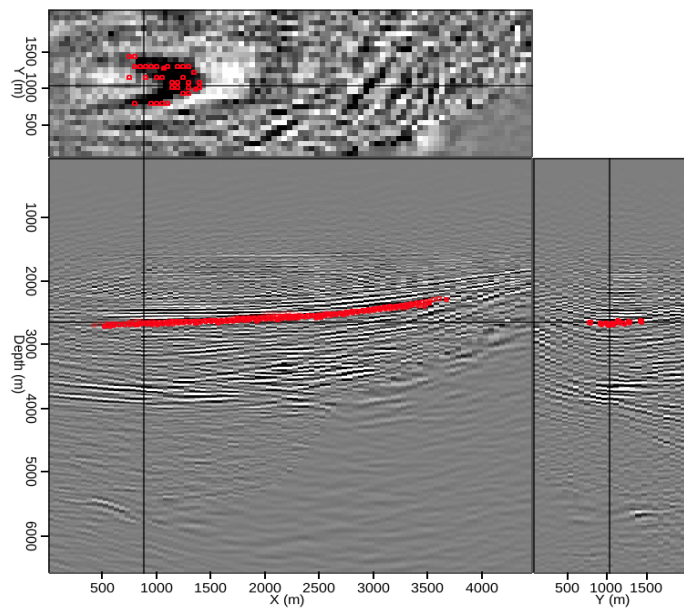


Figure 3.22: Subsurface offset images extracted from the indicated locations in Figure 3.21. The images were created using (a) the slower velocity; (b) the provided velocity; and (c) the faster velocity. [CR] `chap3/. hxy-as,hxy-aa,hxy-af`

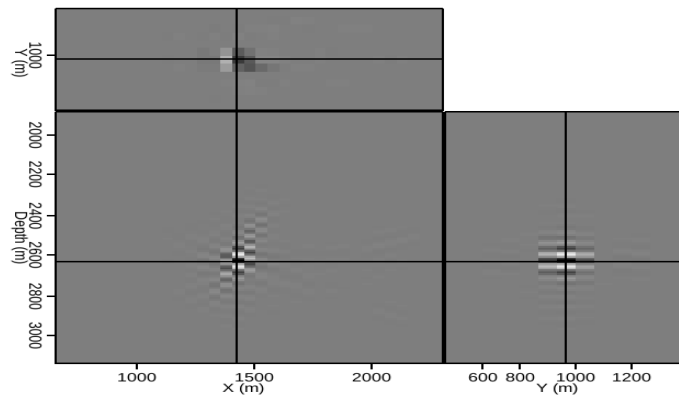


(a)

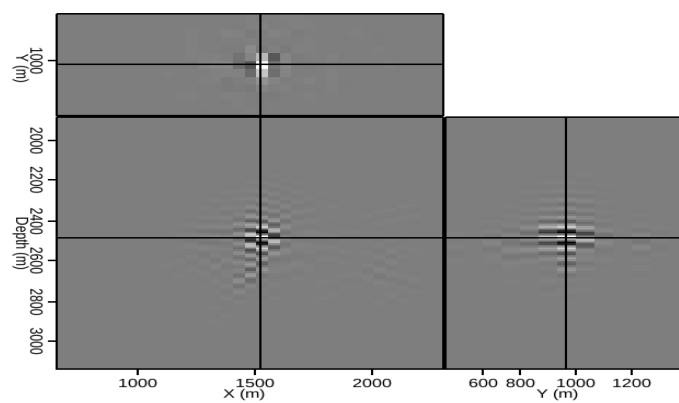


(b)

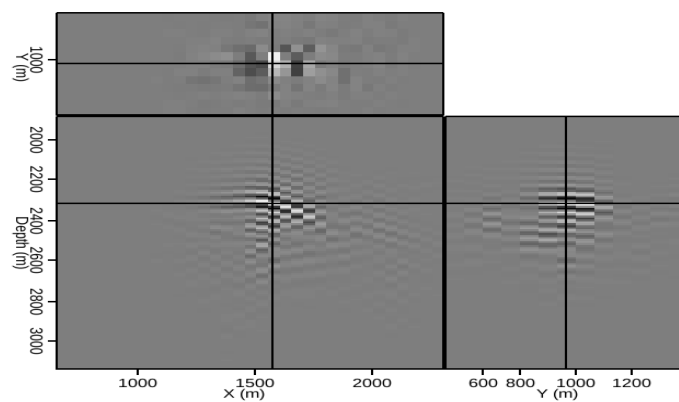
Figure 3.23: (a) A 3D field image produced using a velocity model 5% faster than the one provided, and (b) a manually-picked horizon of interest used to test three different velocity models. [CR] chap3/. 3d-fast,3d-fast-picks



(a)



(b)



(c)

Figure 3.24: A single location from the reflector indicated in Figure 3.23(b), imaged using synthesized source and receiver wavefields and (a) a velocity model 5% faster than the one provided; (b) the provided velocity model; and (c) a model 5% slower than the one provided. [CR] chap3/. fast-fast,fast-act,fast-slow

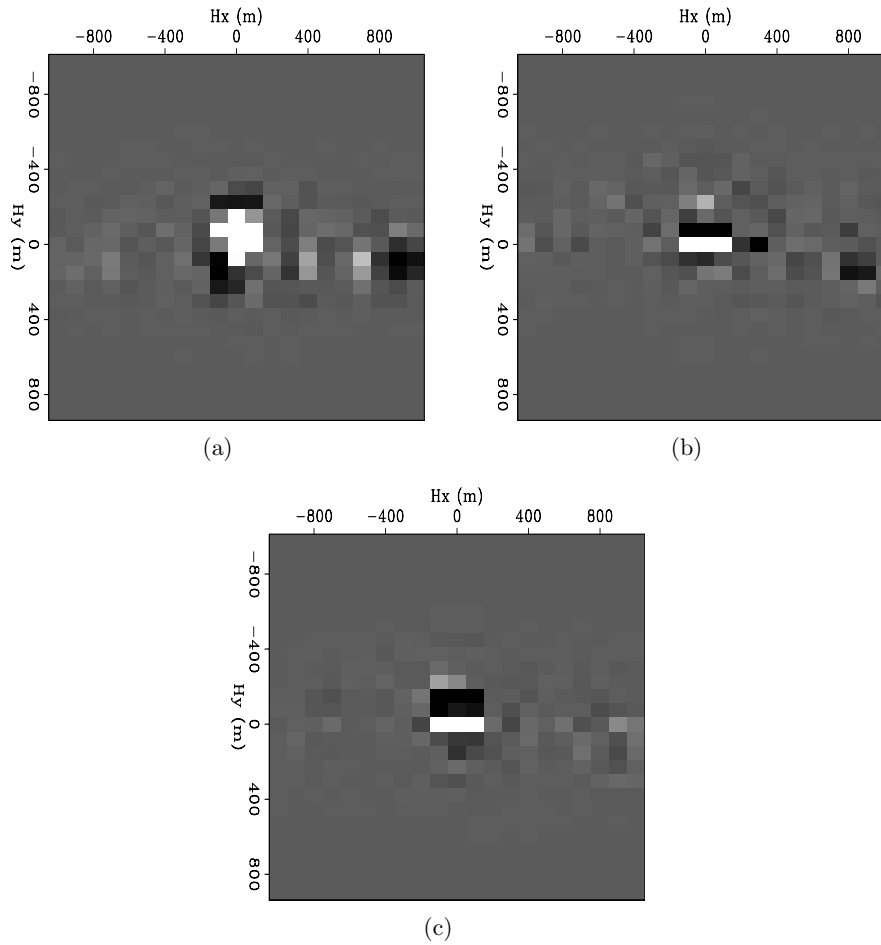


Figure 3.25: Subsurface offset images extracted from the indicated locations in Figure 3.24. The images were created using (a) the faster velocity; (b) the provided velocity; and (c) the slower velocity. [CR] `chap3/. hxy-ff,hxy-fa,hxy-fs`

CONCLUSIONS

This chapter introduced Born modeling techniques, modified to include a source function generated from an initial image, as a means to quickly evaluate multiple possible migration velocity models. By “exploding” subsurface offset gathers from an initial migrated image, we can generate an areal source function with information about the initial velocity model. More importantly, this source function is used to both generate Born-modeled data from isolated points in the subsurface, and to migrate that data to form an image. While crosstalk issues limit implementation of this method to single reflectors, multiple experiments performed on different image locations or reflectors may be used to overcome this limitation. Overall, this method can quickly and accurately reproduce useful velocity information (in the form of subsurface offset gathers) consistent with that obtained from a full migration of the original data. Furthermore, the method allows for re-datuming of wavefields prior to imaging, and can clearly distinguish between velocity models that differ only slightly. This method could form the basis for an efficient and interactive model-building tool, especially when paired with an image segmentation tool like the one presented in Chapter 2.

ACKNOWLEDGMENTS

I thank Schlumberger Multiclient for providing the field dataset used demonstrate the method, and SmaartJV for the Sigsbee synthetic model. I am also extremely grateful to Yaxun Tang for his guidance and prior work on the Born modeling and migration framework used extensively here.